

## A new sensitivity-controlled focusing regularization scheme for the inversion of induced polarization data based on the minimum gradient support

R. Blaschek<sup>1</sup>, A. Hördt<sup>1</sup>, and A. Kemna<sup>2</sup>

### ABSTRACT

We present a new application of a focusing regularization scheme for the inversion of resistivity and induced polarization (IP) data that supports large resistivity magnitude and phase contrasts. Similar approaches so far have only been used for the interpretation of gravity, magnetic, or seismic data sets. Unlike methods based on smoothness constraints, the approach is able to resolve sharp boundaries of bodies and layers, and it allows slight parameter variations within them. Therefore, it can be used in hydrogeologic applications where we need focused images to resolve high-contrast aquifer boundaries. Our approach is based on the minimum gradient support, which seeks to minimize the occurrence of parameter contrasts, independent of their magnitude. We study the effects of a variable control parameter on the reweighting optimization, allowing a continuous transition from smooth to sharp images. We also take the spatially varying sensitivity into account to allow focusing even where sensitivities are small. The implemented weighting leads to increased smoothing in well-resolved areas and a decrease in regions of lower sensitivity. The opposite approach is examined as well. This gradient-dependent sensitivity weighting is basically an extension of depth-dependent sensitivity weighting. We demonstrate the effectiveness and limitations of the approach and the influence of the control parameter using different synthetic models and field data from a hydrogeophysical test site. The technique has proven particularly suitable for revealing sharp parameter contrasts.

### INTRODUCTION

Over the last few years, there has been an increasing interest in the application of the induced polarization (IP) method, in particular in

the spectral IP (SIP) method, as an imaging technique for hydrogeologic and environmental problems (e.g., Slater and Lesmes, 2002; Slater and Glaser, 2003). This is because of its better characterization capabilities compared to pure resistivity surveys. Our overall aim in this paper is to determine hydraulic conductivities at the field scale using empirical relationships, as suggested by Börner et al. (1996). Therefore, we are particularly interested in the impact of regularization on the determination of the phase shift, which has a number of different properties compared to the inversion of dc resistivity only. So far, only a few laboratory studies have been conducted on complex resistivity imaging (the frequency-domain IP approach; e.g., Kemna et al., 2000; Chambers et al., 2004), and corresponding case histories at the field scale (e.g., Kemna et al., 2004) are more rare, particularly with regard to spectral applications (e.g., Kemna et al., 1999; Hördt et al., 2007).

The subsurface structure in hydrogeologic situations often consists of well-defined lithological units with distinctly different properties, such as aquifers and aquicludes. Conventional electrical imaging schemes, however, are based on a standard smoothness constraint, which produces blunted and blurry images that only poorly reflect the reality of such situations. To overcome this insufficiency, various approaches have been suggested to produce images with sharp boundaries. Smith et al. (1999) propose restricting the parameter space by describing the subsurface as a 2D model consisting of variable layers, where the electrical conductivities and depths of each layer are given at a set of nodes and the parameters are interpolated laterally between them. The aim is to find the model with the least lateral variations in depth and resistivity of the layers. Auken and Christiansen (2004) present a similar approach that includes a priori information, and they discuss the advantages and disadvantages of the inversion for layer depths or thicknesses. DeGroot-Hedlin and Constable (2004) suggest an algorithm that only inverts for the layer depths and includes lateral smoothing, whereas the number of layers and their resistivities remain fixed. Yoshioka and Zhdanov (2005) invert SIP data in 3D for Cole-Cole parameters, using both a

Manuscript received by the Editor 6 February 2007; revised manuscript received 7 September 2007; published online 10 January 2008.

<sup>1</sup>Technical University Braunschweig, Department of Applied Geophysics, Germany. E-mail: r.blaschek@tu-bs.de; a.hoerdt@tu-bs.de.

<sup>2</sup>University of Bonn, Department of Applied Geophysics, Germany. E-mail: kemna@geo.uni-bonn.de.

© 2008 Society of Exploration Geophysicists. All rights reserved.

smooth and focusing regularized inversion to generate more reliable images of the subsurface structures.

In this paper, we present a regularization scheme that allows both sharp contrasts between different zones and smooth variations within them, without assuming a layered subsurface at any point along the profile. We use the approach described by Portniaguine and Zhdanov (1999), known as “minimum gradient support” (MGS), as our basis. The main idea here is to penalize parameter differences between adjacent cells, nearly independent of their magnitude. Only if the parameter gradient equals zero is there no penalty. As a consequence, the model with the smallest number of edges in the image is chosen. The result is an extremely sharp image. The MGS approach is a modification of the minimum support functional that was first considered by Last and Kubik (1983). They intended to minimize the volume of an anomalous body in gravity inversion and obtained very compact structures and homogeneous bodies and layers using this stabilizer. Because we wanted to allow smooth variations within the compact structures, we modified the original MGS approach and varied the otherwise small (leading to sharp images) and fixed control parameter to higher values. This is an extension of the analyses of Portniaguine and Zhdanov (1999, 2002), and Portniaguine (1999). Moreover, we took account of the spatially varying sensitivity of resistivity and IP methods in order to achieve some extra focus in regions of lower sensitivity. This idea is based on the approach of Yi et al. (2003), which is known as “active constraint balancing.” Similar studies of depth-varying sensitivity weighting have also been carried out by Portniaguine and Zhdanov (2002). The combination of these different approaches leads to a sensitivity-controlled, focused (SCF) regularization that is an appropriate tool for hydrogeologic imaging and can be adapted to other kinds of massively underdetermined or severely nonunique inverse problems.

## FORMULATION OF THE INVERSE PROBLEM

Any geophysical inversion scheme tries to find a model of the subsurface that explains the measurements. Because of the inherent nonuniqueness of the resistivity/IP inverse problem, the inversion procedure must be regularized by additional constraints to find a unique model with some specific predefined characteristics. One way of solving ill-posed inverse problems is the Tikhonov approach (Tikhonov and Arsenin, 1977). Mathematical formulation of this approach is a minimization of Tikhonov parametric functional

$$\Psi(m) = \Psi_d(m) + \lambda \Psi_m(m). \quad (1)$$

In this equation,  $m$  is the vector of the given model parameters,  $\Psi_d$  denotes a norm of the weighted difference between observed and predicted data,  $\Psi_m$  is the stabilizing functional, and  $\lambda$  is a real, positive number known as the regularization parameter (inversely corresponds to the Lagrange multiplier in constrained optimization theory).

Our software implementation of the IP inverse problem is based on the code by Kemna (2000) and Kemna and Binley (1996). It is a 2D complex resistivity inversion scheme using a finite-element formulation of the forward problem and complex calculus in the inversion algorithm. It minimizes the global objective function

$$\Psi(m) = (d - f(m))^H W_d^H W_d (d - f(m)) + \lambda m^H W_m^T W_m m \quad (2)$$

iteratively by the Gauss-Newton method. The Hermitian is denoted by  $H$ ,  $W_d$  is the data weighting matrix, and  $W_m$  the model weighting

matrix, the latter containing information on the constraint used for the inversion. The operator of the forward solution is described by  $f$ ,  $d$  the data vector. The term  $W_d$  is a diagonal matrix with the inverse of the individual entries being the standard deviation of the applied noise, i.e., the complex data errors  $\varepsilon_i$ :

$$W_d = \text{diag}(1/\varepsilon_1, \dots, 1/\varepsilon_N). \quad (3)$$

Note, that all stabilizing functionals used in the following can be written as the squared  $L_2$  norm of some function of the model parameters (see Portniaguine and Zhdanov, 1999, 2002; Zhdanov, 2002). We used this reweighted formulation to convert Tikhonov parametric functional (equation 1) into quadratic form as shown in equation 2.

Our inversion uses the conjugate gradient method to solve for model updates. The inversion starts with a homogenous half-space model. The conductivity of this half-space is determined as the weighted (by standard deviation) mean of the log-scaled apparent conductivities of each measured value. (A typical data misfit is  $\text{rms} = 50$  for the half-space starting model). The starting value for  $\lambda$  is estimated according to the suggestions of Newman and Alumbaugh (1997).

The value of  $\lambda$  is changed during the inversion. At each inverse iteration step, a univariate search is performed to find the maximum value of the regularization parameter that locally minimizes the data misfit function (or, respectively, yields the desired target misfit); details can be found in Kemna (2000). The approach is similar to that employed by deGroot-Hedlin and Constable (1990) and later adapted by Oldenburg et al. (1993) and LaBrecque et al. (1996).

## THE MINIMUM-GRADIENT-SUPPORT REGULARIZATION APPROACH

Generally, an infinite number of models that fit the data equally well exists, and the preferred solution depends on the additional constraints applied. For comparative purposes, we introduce the widely used smoothness constraint, where  $\Psi_m$  is the integral over the  $L_2$  norm of the model gradient (deGroot-Hedlin and Constable, 1990):

$$\Psi_{m,L_2}(m) = \int_V \|\nabla m\|^2 dv. \quad (4)$$

Here, the contribution to the model objective function increases with the square of the model gradient. An inversion using this constraint is also referred to as Occam's or smoothness-constrained inversion. Alternatively, the  $L_1$  norm may be chosen (e.g., Loke et al., 2003):

$$\Psi_{m,L_1}(m) = \int_V \|\nabla m\| dv. \quad (5)$$

The  $L_1$  norm increases only linearly with the model gradient and thus produces more blocky models than the  $L_2$  norm because the penalty for larger gradients is smaller. The aim of the above approaches are similar to the regularization suggested in this paper, but there are essential differences.

According to Portniaguine and Zhdanov (1999), the minimum-gradient-support functional can be written as

$$\Psi_{m,\text{mgs}}(m) = \int_V \frac{\nabla m \cdot \nabla m}{\nabla m \cdot \nabla m + \beta^2} dv. \quad (6)$$

For small values of  $\beta$ , the functional behaves like a step function, as can be seen from

$$\lim_{\beta \rightarrow 0} \frac{\nabla m \cdot \nabla m}{\nabla m \cdot \nabla m + \beta^2} = \begin{cases} 0 & \text{for } \nabla m = 0 \\ 1 & \text{for } \nabla m \neq 0 \end{cases} \quad (7)$$

Portniaguine and Zhdanov (1999) use a small but fixed value for  $\beta$ . In this case, very small variations are penalized in the same way as very large ones, and one obtains blocky models where zones with no parameter variation inside are separated from each other by sharp contrasts. An extreme application is found in Portniaguine and Castagna (2004), where, in a seismic application,  $\beta$  is set to  $10^{-8} \max(m)$  (related to machine precision) in a variation of the minimum support constraint. More detailed explanations on stabilizing functionals can also be found in Zhdanov (2002).

We are particularly interested in the inversion of IP data, which could be applied to hydrogeologic problems. We want to maintain the well-separated zones, but at the same time we wish to allow smooth parameter variations within them. Therefore, we recommend setting an intermediate value for  $\beta$ . First, we note that in the limit of large  $\beta$ , the function asymptotically converges toward a penalty proportional to the  $L_2$  norm:

$$\beta \gg \nabla m \Rightarrow \frac{\nabla m \cdot \nabla m}{\nabla m \cdot \nabla m + \beta^2} \approx \frac{\nabla m \cdot \nabla m}{\beta^2} \propto \nabla m \cdot \nabla m. \quad (8)$$

Consequently, by exploring different values of  $\beta$ , we can generate a continuous transition between sharp and smooth models.

Figure 1 shows the regularization term as a function of the model gradient for different values of  $\beta$ . This is normalized by some  $\beta_0$ , which may be considered arbitrary at this stage. For comparison, the  $L_1$ - and  $L_2$ -norm functions are displayed as well.

Parameter gradients with a steep slope tend to be unstable, because a small decrease in the parameter gradient (with little effect on the data misfit) leads to a large decrease in the contribution to the regularization term where the slope is steeper.

Between the  $L_1$  and  $L_2$  norm, there are two sections that exhibit qualitatively different behavior: for smaller parameter gradients, the  $L_2$  norm is less steep; for larger gradients, the  $L_1$  norm is less steep. As a result, higher gradients are more stable for the  $L_1$  norm, and lower gradients are more stable for the  $L_2$  norm. The  $L_2$  norm therefore leads to smoother images.

The MGS function exhibits a mixed behavior with three sections. For large parameter gradients, the slope is extremely small and runs into saturation, leading to stable values. For intermediate values, the curve is steep and values are thus unstable in this region. For very low parameter gradients (Figure 1b, case  $\beta = \beta_0$  shown), the curve flattens again and stable gradients are obtained. The result is a blocky model with sharp contrasts between the blocks and smooth variations within the structures, which makes the MGS functional fundamentally different from both the  $L_1$  and the  $L_2$  norms.

By varying  $\beta$ , the ranges of the different regions of stability can be changed. Here, with a large  $\beta$ , we obtain a curve similar to the  $L_2$  norm for parameter gradients of interest. In Figure 1, the curves for  $\beta = 10 \beta_0$  and the  $L_2$  norm con-

verge rapidly for small parameter gradients. Decreasing  $\beta$  results in more focused images.

To illustrate the influence of  $\beta$ , we used a simple model consisting of a rectangular dike of 10  $\Omega\text{m}$ ,  $-15$  mrad, embedded in a homogeneous half-space of 100  $\Omega\text{m}$ ,  $-5$  mrad (Figure 2). Synthetic data were calculated for a profile crossing the dike in a perpendicular direction with a dipole-dipole configuration with 2 m dipole spacing and 33 electrodes. Data were used up to a dipole spacing of  $n = 14$ , and Gaussian noise was added to the data (1% magnitude, 0.3 mrad phase, uncorrelated). This is the order of typical data misfits estimated from the inversion of field data. The subsurface was parameterized using a grid of rectangular blocks of size  $0.5 \times 0.5$  m for the forward calculation and  $0.67 \times 0.67$  m for the inversion. This was done to avoid a favorable bias in the inversion that might result from using identical grids for both modeling and inverting the data.

First, the inversion was carried out using a large value of  $\beta$ , i.e.,  $\beta = 10 \beta_{\text{opt}}$ . As expected, a smooth model is obtained (Figure 3a and b) where the body is at the correct location, but the boundaries are not well recovered and the parameter contrast is too low. The variations in the background are caused by the Gaussian noise added to the data. In the next step,  $\beta$  was decreased by a factor of

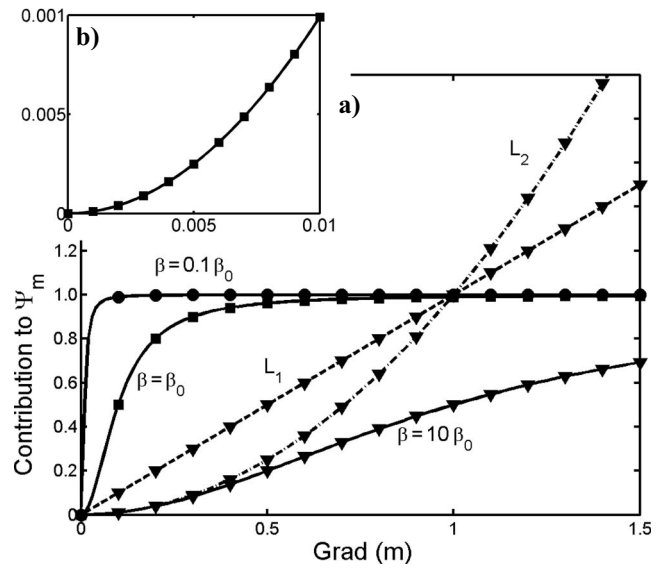


Figure 1. Regularization kernel as a function of the model gradient for the  $L_1$  and  $L_2$  norms, and the MGS functional for three different values of  $\beta$  with reference value  $\beta_0$  (i.e., kernel in equations 4–6); b) cut-out around 0 for  $\beta = \beta_0$ .

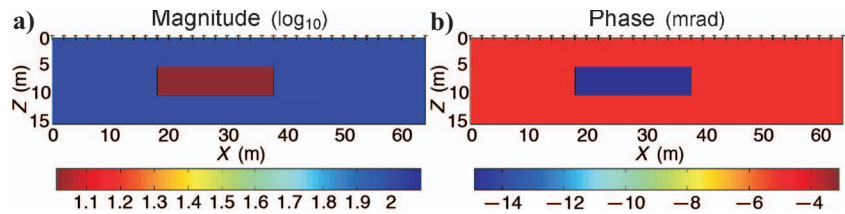


Figure 2. Model with a rectangular block embedded in a homogeneous half-space. The parameters of the block are 10  $\Omega\text{m}$  and  $-15$  mrad, the half-space parameters are 100  $\Omega\text{m}$  and  $-5$  mrad.

10 ( $\beta = \beta_{\text{opt}}$ ). The resulting image is much more similar to the original model (Figure 3c and d). Both magnitude and phase show almost the correct contrast (more than 80% in magnitude and phase), and the edges of the body are also close to the true ones. However, it should be noted that the edges cannot be perfectly reproduced because different parameterizations were used for modeling and inversion and the result can therefore be considered satisfactory. Attempts to reproduce the true model better by decreasing  $\beta$  further failed. As shown in Figure 3e and f, for  $\beta = 0.1 \beta_{\text{opt}}$ , the lower edge is no longer recovered. The inverted model consists only of two nearly homogeneous regions, and the body is extended downward to the bottom of the inversion grid. This is because the inversion has further minimized the number of edges associated with nonzero parameter gradients. Because of the fact that a larger region is now assigned to the body, the contrast decreases again.

We conclude that the optimum  $\beta$  for this blocky model is not  $\beta \rightarrow 0$  but rather a finite value. Furthermore, this value does not depend on the underlying grid, as the dimension ( $\text{m}^{-1}$ ) already compensates

for geometry (e.g., a parameter change of 10% over 5 m is independent of the discretization).

For various synthetic models (combinations of bodies, layers, and smooth transitions with different contrasts) we estimated the  $\beta$  value with the smallest difference between the inversion result and the true model (not to be confused with measured and calculated data). This study led to the conclusion that an optimal  $\beta$  exists that can be applied to a wide range of different models. Our recommended value is  $\beta_{\text{opt}} = 0.3 \text{ m}^{-1}$ . The maximum slope of the curve in Figure 1, where the gradient is least stable (i.e., where the penalty shows the highest sensitivity to changes in the gradient), belongs to a value of the gradient of  $\beta/\sqrt{3}$  (corresponding to the maximum of the first derivative with respect to  $\nabla m$ ). For  $\beta = 0.3 \text{ m}^{-1}$ , this means that the most unstable gradient is approximately  $0.17 \text{ m}^{-1}$ . Because the parameters consist of log-transformed resistivities, this value represents a gradient relative resistivity of around 19%  $\text{m}^{-1}$  in linear scale ( $\exp(0.17) \approx 1.19$ ). The slope decreases to half of the maximum value for changes of about 5% and 52%  $\text{m}^{-1}$ . This means that gradients of 52%  $\text{m}^{-1}$  are as stable as those of 5%  $\text{m}^{-1}$ .

Instead of using a standard value for  $\beta$ , it is also possible to scan through a range of different values and select the result that corresponds best with available a priori information on the model. This is especially recommended for models with extremely high or low expected contrasts (compared to the following examples). A more rigorous approach for the calculation of an optimum  $\beta$  is given in Zhdanov and Tolstaya (2004), where  $\beta$  is estimated using the starting model.

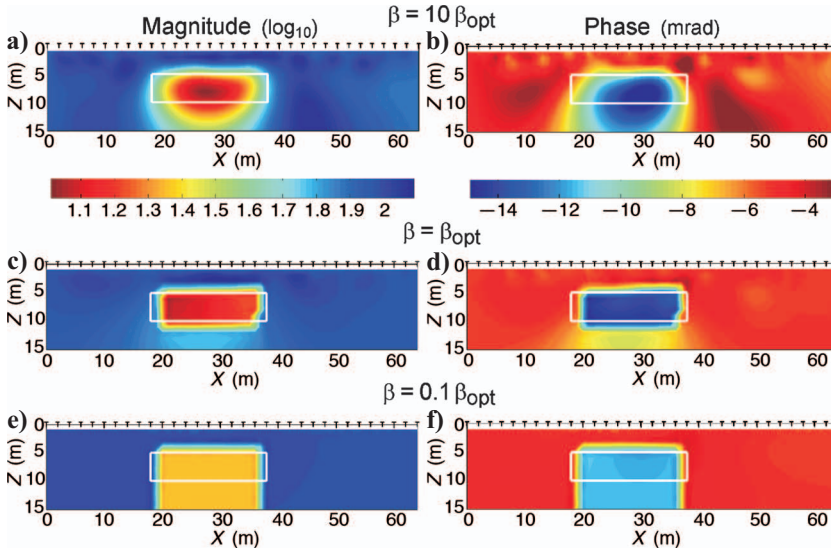


Figure 3. Inversion results employing MGS regularization for the model shown in Figure 2. The true position of the block is indicated by the white rectangles. (a–f) display results for different values of the control parameter  $\beta$  ( $\beta = 10 \beta_{\text{opt}}$ ,  $\beta = \beta_{\text{opt}}$ ,  $\beta = 0.1 \beta_{\text{opt}}$ , respectively).

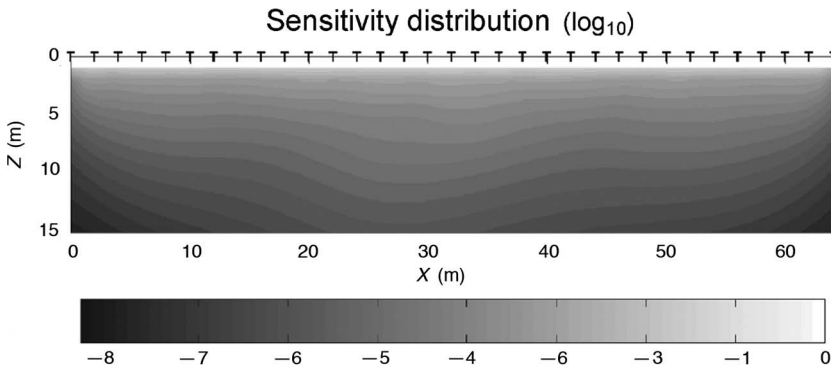


Figure 4. Spatial distribution of accumulated squared absolute sensitivity, normalized to the maximum value that occurs, as defined in equations 9 and 10 in logarithmic ( $\log_{10}$ ) scale.

## DEPENDENCE ON SENSITIVITY VARIATION

Even with an optimal value for  $\beta$ , the contrast at the lower boundary of the body is not well resolved. In Figures 3c and d, there are still small shadow effects below the conductive body, which are particularly apparent in the phase image. One reason for this is the lower sensitivity in this region. Figure 4 illustrates the huge dynamic range of the accumulated sensitivity (coverage) for the simulated dipole-dipole survey with 33 electrodes, 2 m dipole lengths, and dipole spacings  $n = 1, \dots, 14$ . The asymmetric distribution is caused by the underlying model (see Figure 2). The accumulated sensitivity for parameter cell  $j$ ,  $g_j$  is defined as the weighted sum of the squared absolute complex sensitivity over all measurements  $i = 1, \dots, n$  (Kemna, 2000):

$$g_j = \sum_{i=1}^n s_{ij} \overline{s_{ij}} / d_i \overline{d_i} = \sum_{i=1}^n |s_{ij}|^2 / |d_i|^2. \quad (9)$$

In equation 9,  $\overline{\phantom{x}}$  denotes complex conjugation. The variable  $s_{ij}$  is the sensitivity of the logarithm of the  $i$ th impedance measurement  $V_i$  with respect



to the logarithm of the conductivity  $\sigma_j$  of the  $j$ th parameter cell,

$$s_{ij} = \frac{\partial \ln V_i}{\partial \ln \sigma_j}. \quad (10)$$

A complex data error is described by  $d_i$  (error ellipse around the data point  $\ln V_i$  in the complex plane) and contains the standard deviation of the log resistance data in its real component and the standard deviation of the impedance phase in its imaginary component (Kemna, 2000). The distribution of  $g_j$  values, normalized to the maximum value, is shown in Figure 4 in logarithmic scale. The values decrease by a factor of approximately  $10^{-6}$  or more from the surface to the lower boundary of the body.

The sensitivity should be taken into account in order to sharpen the image at the bottom of the body. We will begin with the  $L_2$ -norm regularization to illustrate the effect with well-known smoothness-constrained images.

### Incorporation into smoothness constraint

Two different approaches may be considered with regard to taking the sensitivity information into account in the regularization. The first idea, which was applied by Yi et al. (2003), for example, is to attribute less weight to the smoothing functional in regions of high sensitivity, because these regions only require a relatively weak constraint to stabilize the system. In regions of low sensitivity, the regularization should play a more dominant role, and therefore the weights of the smoothing functional should be increased here. Yi et al. (2003) determine the Lagrangian multiplier via the parameter resolution matrix and spread function analysis. We modified this implementation by using a function that depends only on  $g$  (equation 9). Further information about reweighted optimization can also be found in Portniaguine and Zhdanov (2002) and Portniaguine (1999), where a depth-dependent sensitivity weighting is used. Our approach of gradient-dependent sensitivity weighting can be seen as an extension of this.

In our implementation, we define a sensitivity-dependent function that refers to an edge between two adjacent cells  $j$  and  $k$ . Because of the large dynamic range, the logarithm of  $\bar{g}$  is used, where  $\bar{g}$  is defined as the spatial average value over all  $g_j$  values ( $\bar{g} = 1/l \sum_{j=1}^l g_j$ ). We then define the function  $f(j,k)$  as:

$$f(j,k) = 1 + \left( \frac{1}{|\log_{10}(\bar{g})|} (|\log_{10}(g_j)| + |\log_{10}(g_k)|) \right). \quad (11)$$

As the maximum value of  $g_j$  is 1, the minimum value of the sum in the brackets becomes 0, and, correspondingly,  $f(j,k)$  is always  $>1$  and increases with decreasing sensitivity. The additional 1 is a stabilizing term that limits the dynamic range and helps to avoid zero values, particularly for implementation into the MGS function and the following second approach. The function  $f(j,k)$  is now used as a factor for the regularization parameter. Figure 5c and d illustrate the ef-

fect of this implementation for the synthetic model considered in this paper. In this case, asymmetry and artifacts are caused by noise that has been added to the data (the same as for the previous  $\beta$  study). When compared to the standard inversion result with smoothness-constraint regularization (Figure 5a and b), the resolution of the body, and its bottom in particular, significantly decreases as expected.

The second way to incorporate sensitivities into the regularization is to increase smoothing in well-resolved areas and decrease it in regions of lower sensitivity. The reasoning behind this is that there is the risk of producing artifacts in well-resolved areas when over-fitting the data (i.e., below the noise level). Increased smoothing may reduce this effect. In regions of low sensitivity, a structure that appears during the inversion process starting from a homogeneous half-space is not likely to be artificial and should not be destroyed by excessive smoothing. Of course, one risk associated with this approach is that it may favor artifacts in low sensitivity regions. A typical result is shown in Figure 5e and f. Compared to the standard smoothness inversion (Figure 5a and b), decreased smoothing in low sensitivity regions produces a body that is better resolved. Although the opposite weighting of sensitivity (Figure 5c and d) produces fewer artifacts, it still fails to resolve the body well.

We did not make an attempt to study the effect of systematic errors, because they are very difficult to predict and can lead to misinterpretation, not only for our particular regularization. Because our final aim is to determine the hydraulic conductivities of aquifers in regions where a priori information on lithology is usually available and the risk of undetected large-scale artifacts is low, we proceeded to implement the sensitivity-dependent regularization into the MGS functional.

### Incorporation into minimum gradient support

We now combine the minimum gradient support with the focusing version of the sensitivity dependence. The modification is carried out as:

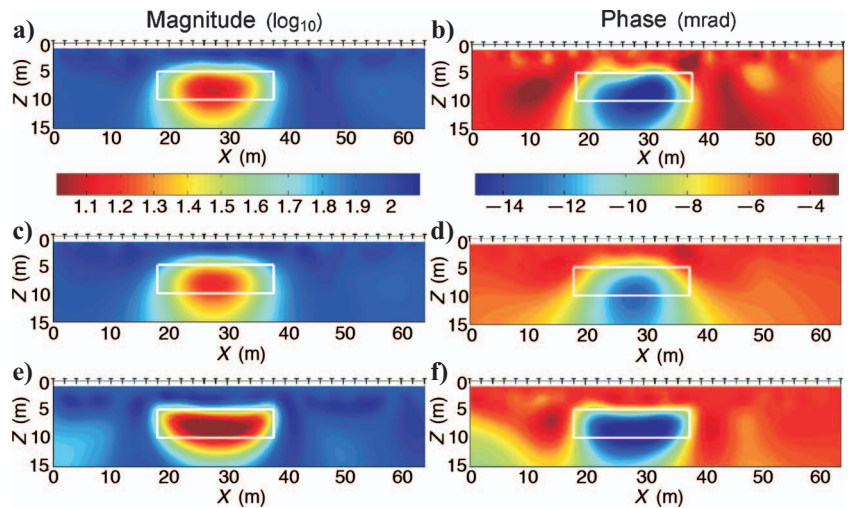


Figure 5. Smoothness-constrained inversion results for the model shown in Figure 2 using different methods to incorporate sensitivity information into the regularization. (a and b) No sensitivity information used. (b and c) Increased smoothing with decreasing sensitivity; (e and f) decreased smoothing with decreasing sensitivity.

$$\frac{(\nabla m_{ij})^2}{(\nabla m_{ij})^2 + \beta^2} \Rightarrow \frac{1}{f(i,j)^2} \frac{(\nabla m_{ij})^2}{(\nabla m_{ij})^2 + \left(\frac{\beta}{f(i,j)}\right)^2}, \quad (12)$$

with  $\nabla m_{ij} = |m_j - m_i|/w(i,j)$  and  $w(i,j)$  the distance between the centers of cells  $i$  and  $j$ . The effect in low sensitivity regions ( $f \gg 1$ ) is that the focusing is intensified (change in denominator leads to smaller effect of  $\beta$ ), whereas the overall contribution to the objec-

tive function decreases. The net effect is that the functional does not change for small gradients, but for large gradients, where an increase in the gradient is not penalized any heavier, and saturation is reached more easily. In the following, we will call this kind of regularization the SCF inversion. Aspects of incorporating the sensitivities into the regularized focusing inversion are also discussed in Zhdanov (2002).

Figure 6 shows the effect of the SCF inversion on the synthetic example. Clearly, the target boundaries are resolved better, both in the resistivity and phase images. The shadow zone below the body (compare Figure 3c and d), for example, no longer exists. At the same time, no additional artifacts have appeared. On the contrary, the number of artifacts has even been slightly reduced in the region above the body. This may be because of the relatively smaller weight in those regions, which would mean that data errors do not lead to near-surface spatial variation as readily as before.

The data misfit is evaluated in terms of a weighted rms error. An ideal fit of  $\text{rms}=1$  occurs when the absolute value of the average difference between the measured and calculated data equals the standard deviation of the data. This is used as the stopping criterion in the inversion, and was achieved in all of the synthetic examples. We further evaluated the inversion results by looking at the spatial distribution of the data (apparent complex resistivity) residuals. These residuals should be random, in accordance with the synthetic noise added. Figure 7 shows pseudosections for the inversion results of Figure 6. In the bottom row, the deviations for magnitude and phase of the apparent complex resistivity data are given for the SCF inversion result. The phases behave in a rather unstructured manner, while the higher deviations of the magnitudes are clustered in a small region associated with the position of the block. Maximum values are between 8% and 10%. The smoothness-constrained inversion results (Figure 7a and b) show a similar distribution for the phases, but a stronger accumulation of high deviations of up to 18% in magnitude. SCF regularization therefore also results in a more favorable distribution of the individual data residuals.

The model with a single isolated body (Figure 2) was used to illustrate some basic properties of the different regularization approaches. In order to assess the new algorithm in a more realistic situation, we constructed a more complex model as shown in Figure 8. The model consists of three layers, where the middle layer has a minimum resistivity, and the (absolute) phases increase with depth. The depth of the middle layer decreases from left to right. Two blocks of moderate contrast are embedded in the middle layer. This model aims to show the possible resolution of a more conductive layer above a more resistive one and vice versa. The slight variations within the second layer pose an additional challenge.

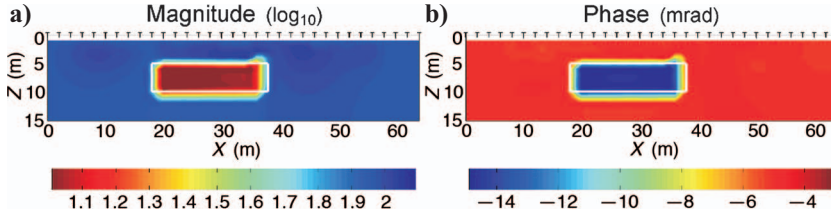


Figure 6. Inversion results for the model shown in Figure 2: Enhanced focusing in low-sensitivity regions using sensitivity-controlled focusing (SCF) inversion (compare Figure 3c and d where no sensitivity information was used).

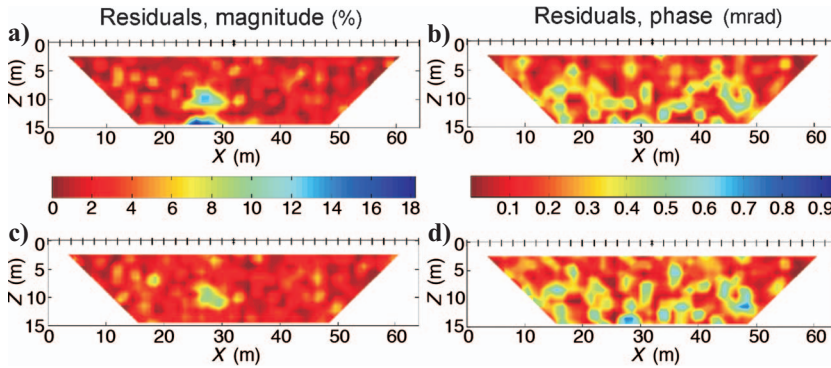


Figure 7. Spatial distribution of the residuals of the apparent complex resistivity data for the inversion results shown in Figure 6. (a and b) Smoothness-constrained inversion. (c and d) SCF inversion.

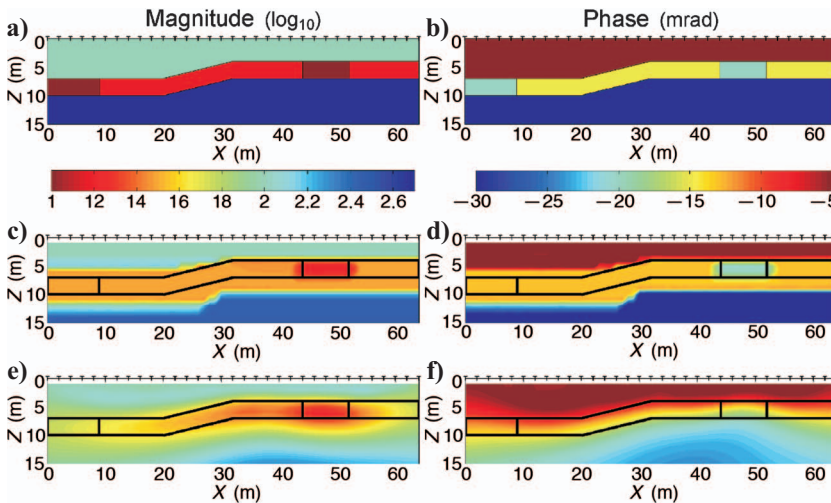


Figure 8. Three-layer synthetic model. (a and b) Model with top layer 100  $\Omega\text{m}$ ,  $-5$  mrad; second layer 15  $\Omega\text{m}$ ,  $-15$  mrad (two blocks with 10  $\Omega\text{m}$ ,  $-20$  mrad); and lower half-space 500  $\Omega\text{m}$ ,  $-30$  mrad. (c and d) SCF inversion result. (e and f) Conventional smoothness-constrained inversion result.

The forward simulation was done with a triangular grid allowing for dipping boundaries, whereas the inversion was carried out with rectangular  $0.5 \times 0.5$  m cells. The simulated measurement configuration was the same as above: 33 electrodes with 2 m electrode separation, a dipole-dipole configuration with 2 m dipole length up to  $n = 14$ , leading to 33 receiver channels and 329 different combinations of injection and measurement dipoles (i.e., impedance data). Synthetic Gaussian noise with a standard deviation of 1% (magnitude) and 0.3 mrad (phase) was added to the data, uncorrelated between magnitude and phase.

Inverting the synthetic data using the SCF regularization leads to a reasonable reconstruction of the input model (Figure 8c and d). All three layers are clearly resolved. However, the middle layer is slightly smeared out, thus, the contrast is a bit too low. Moreover, the bottom of the middle layer appears 1–2 m too deep. The upper block inside the second layer can be seen in both magnitude and phase. The second body is not resolved, probably because it is located in the low sensitivity region near the boundary of the inversion grid. No artifacts are caused by the application of the gradient sensitivity weighting.

Figure 8e and f shows the smoothness-constrained inversion for comparison. The magnitude image is acceptable to some degree. Except for the left body in the middle layer, all features (the three layers and the second body) are resolved, although the quality is not as good as that produced using the SCF approach. For this type of regularization, boundaries are typically smeared out and the parameter contrasts are too low. The phase image shows a continuous decrease with depth instead of a layering, and the phase values of the bottom layer are too small. Another positive aspect of the SCF approach is that it produces a horizontal continuation of the second layer even in low sensitivity regions where the smoothness constraint leads to a nearly homogeneous model. The overestimation of the thickness of the second layer, by the SCF approach, is more than compensated by the clearer contrast and better values for magnitude and phase. As we need both magnitude and phase values to determine the hydraulic conductivity, the SCF approach leads to considerably better results and is thus preferable.

In order to examine the behavior of the SCF approach when no sharp boundaries are present, a model with gradational changes only was used. The parameters varied in the vertical direction only, and the model was purely 1D, but we used the same geometries and 2D inversion algorithms as in the model above. The parameters changed from  $100 \Omega\text{m}$ ,  $-0.25$  mrad at the surface in small steps (see stepped black curves in Figure 9a and b) to  $10 \Omega\text{m}$ ,  $-15$  mrad (at 20 m, where a half-space follows). From the 2D inversion result, we extracted the parameter variation with depth in the middle of the profile. As expected, the smoothness-constrained inversion (gray curves) fit the model well. The SCF approach (smooth

black curves) had more difficulties in reproducing the model, but it did not create sharp boundaries as one might have expected. Even though the SCF approach is not designed for smooth models (and should not be used if a priori information indicates large-scale gradational changes), it still gives acceptable results in such cases.

## FIELD RESULTS

Measurements may be carried out at different frequencies, in which case the method is SIP. In the field, the usable frequency range is often limited by inductive and capacitive coupling, as well as logistical constraints; this is the reason we consider single-frequency data at this stage. Excellent reviews of the IP method are provided in Bertin and Loeb (1976) and Sumner (1976).

In order to illustrate the practical usefulness of our approach, we discuss its application to field data. The data are from the hydrogeo-

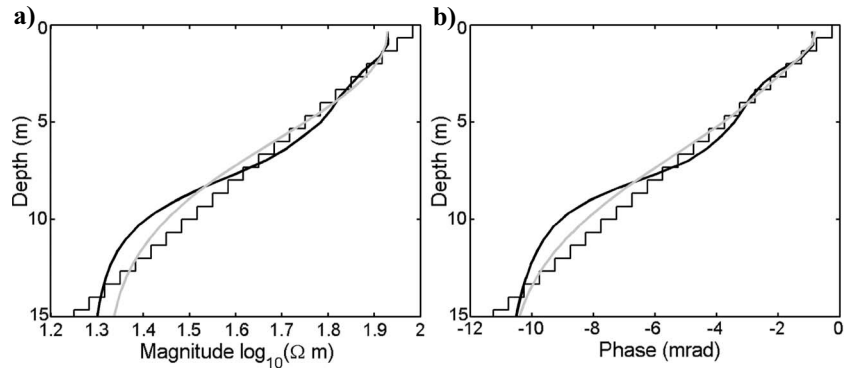


Figure 9. Model (stepped black curves) and inversion result using SCF regularization (smooth black curves) and smoothness constraint (gray curves) for a 1D model with gradational parameter variations. Shown are (a)  $\log_{10}$  of magnitude (in  $\Omega\text{m}$ ) and (b) phase in mrad.

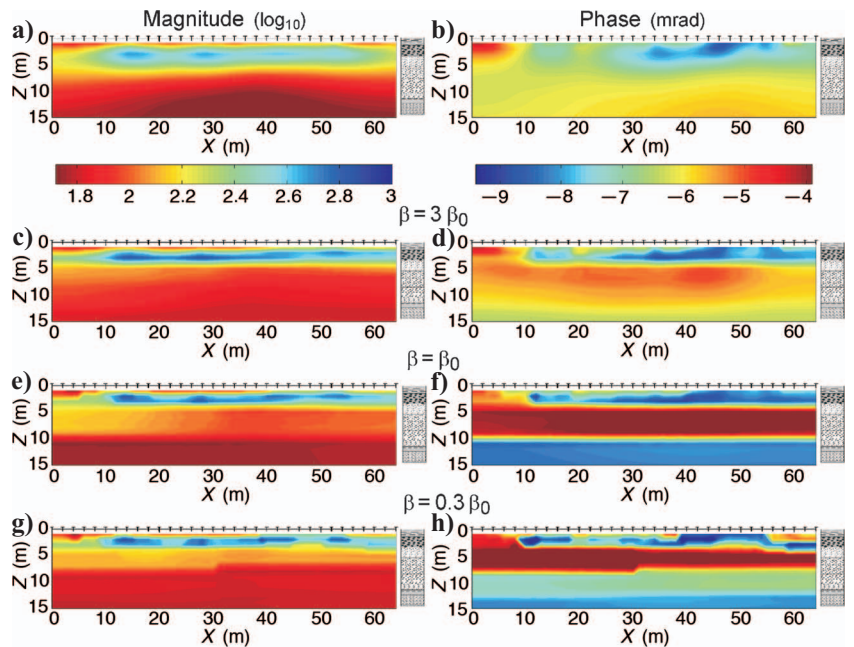


Figure 10. Inversion results obtained from field data collected at the Krauthausen hydrological test site.  $\beta$ -study using SCF regularization. (a and b) Smoothness constraint; (c and d) triple the basic value; (e and f) the basic value; (g and h) 0.3 times the basic value.



logic test site Krauthausen, Germany, which is operated by the Institute of Chemistry and Dynamics of the Geosphere-Agrosphere (ICG-4), Forschungszentrum Jülich (Vereecken et al., 2000). The lithology known from various drillings was mainly 1D, and on average consisted of an approximately 9-m-thick aquifer, a groundwater table at around 2 m, and a surface soil layer above (Figure 10, vertical bars). The aquifer is characterized by different layers of sand and gravel. A clay layer at a depth of approximately 11 m forms the base of the aquifer and is followed by fine sands. The layer between 1.4 and 3.4 m exhibits a strongly nonuniform grain-size distribution (i.e., with both very small and large grains). We therefore expected to see two layer boundaries at depths of about 3.4 and 11.4 m. A third boundary exists close to the surface at a depth of about 1.4 m with a material change from soil to gravel. The sequence should be from a dry resistive top layer through better conducting sand and gravel to good conducting clay. The phase should reach its maximum value in the clay and silty fine sands below the aquifer base.

The SIP data were acquired with the multichannel instrument SIP256C from Radic Research (Radic et al., 1998; Radic, 2004). The profile discussed here was recorded using a dipole-dipole configuration and 32 electrodes at 2 m spacing. We took measurements over a frequency range from 76.22 mHz to 500 Hz, but only single frequency data at about 0.3 Hz will be discussed here. We chose this frequency for its good data quality. Furthermore, the other frequencies led to similar results. Various approaches of multifrequency inversion are shown in Blaschek et al. (2006) and among other aspects discussed in Blaschek (2006). A more detailed description of the entire survey including sample spectra can be found in Hördt et al. (2004, 2005; and 2007).

Like the previous synthetic examples, the depth of investigation is about 15 m. In this particular case, it was given by the field configuration adapted to the depths of the layers in which we are interested. In general, the investigation depth for SIP measurements is limited by induction effects, which become important at large transmitter-receiver spacings (e.g., Telford et al., 1990). As long as induction can be ignored, the conclusions do not depend on the investigation depth, and the previous results may be simply scaled up.

Figure 10e and f shows the inversion results using the SCF regularization with optimum  $\beta$  for magnitude and phase. The agreement between model and average lithology is excellent. The known lithologic boundaries are reflected in both resistivity magnitude and phase at the correct depths. Even the boundary between the near-surface soil and aquifer is visible, in particular in the magnitude image.

The other parts of Figure 10 show the inversion results with smoothness constraint (a and b) and an SCF regularization with (c and d) large and (g and h) small  $\beta$  to illustrate the continuous transition between smooth and blocky models. If a sufficiently large value for  $\beta$  (e.g.,  $\beta = 10 \beta_0$ , not shown here) is chosen, the SCF regularization can produce results that are practically identical to the smoothness-constrained results.

The smoothness-constrained model (Figure 10a and b) only roughly corresponds to the average lithology, and it does not exhibit a sharp boundary at a depth of around 11 m, where the aquifer base is expected. Aquifer and aquifer base cannot be separated. Lateral variations that could be attributed to geology exist only in the top layer (above 5 m). Below 5 m, any variation is dominated by the smoothness constraint and the image is not useful for hydrogeologic applications. On the other hand, the SCF regularization with optimum  $\beta$  (Figure 10e and f) agrees very well with the average lithology. The most striking feature is the boundary at 11 m, corresponding to the

known boundary between aquifer and aquifer base. The advantage of SCF regularization is particularly apparent in the phase images. Whereas the smoothness-constrained inversion does not even produce an increase in phases at depth, the SCF inversion produces a reasonable contrast.

The SCF model also exhibits lateral variation within the aquifer (depth between 5 and 10 m), particularly in the resistivity image. This feature is difficult to assess, because external information on the lateral variation of electrical parameters is not available at this spatial scale. However, it should be noted that the SCF image appears to be slightly less dominated by the regularization than the smoothness-constrained image. A final assessment would be easier in the future when data with stronger lateral variation and more a priori information become available.

The transition between blocky and smooth models is illustrated in Figure 10c, d, g, and h. The result with a moderately large  $\beta$  ( $\beta = 3 \beta_0$ , Figure 10c and d) is slightly sharper than the smoothness-constrained model, but unlike the optimum model in Figure 10e and f, it still does not resolve the sharp boundary at around 11 m. For small  $\beta$  (Figure 10g and h), the model becomes blocky and the contrasts between the different quasihomogeneous zones become unrealistically large.

It should be stressed that the optimal  $\beta_0$  was obtained from studies with synthetic data and not from a comparison with the lithology. We take the good agreement with the lithology as confirmation that  $\beta_0 = 0.3 \text{ m}^{-1}$  also works well with the field data. Depending on the circumstances and the availability of a priori information, different values could be preferred, but our  $\beta_0$  seems to be a reasonable standard value. Nevertheless, for a nonunique problem, a single solution can be dangerously misleading and we recommend scanning through the model space to support the interpretation. As always, the interpreter should resist the temptation to select the model that fits their expectation best and consider it as a representation of the truth.

The data fits for all of the inversion results shown in Figure 10 are identical. As outlined above, they are evaluated in terms of a weighted rms error, and the inversion is stopped when the average difference between the measured and calculated data is equal to the error level in the data. This weighting, however, is not based on the measurement errors provided by the acquisition system, which are determined statistically during the stacking procedure, because these are generally too small and do not reflect geologic noise or other sources of error (e.g., electrode position errors, errors associated with the 2D representation of a 3D subsurface, and modeling errors). Instead, a constant error level of 1% for the magnitude and 0.3 mrad for phase is used. With this definition, the target rms value of 1 is reached in all cases shown here. However, it is still useful to look at the individual data fits because there are differences in their spatial distribution.

First, we look at the pseudosections of measured and calculated data for the smoothness-constrained and SCF inversion results (Figure 11). As expected, the differences between the raw data and the inversion results are marginal. The SCF inversion (Figure 11e and f) seems to fit the phase data slightly better at the left border and for the diagonal features with higher (absolute) phase values that are much weaker in the data predicted by the smoothness-constrained result. The diagonal features in the measured data arise from small-scale structures in the immediate vicinity of the electrodes. The inversion simulates these by introducing near surface parameter contrasts. Because the smoothness constraint prohibits large parameter contrasts between adjacent cells, it may be slightly more difficult to correctly simulate the small-scale structures.



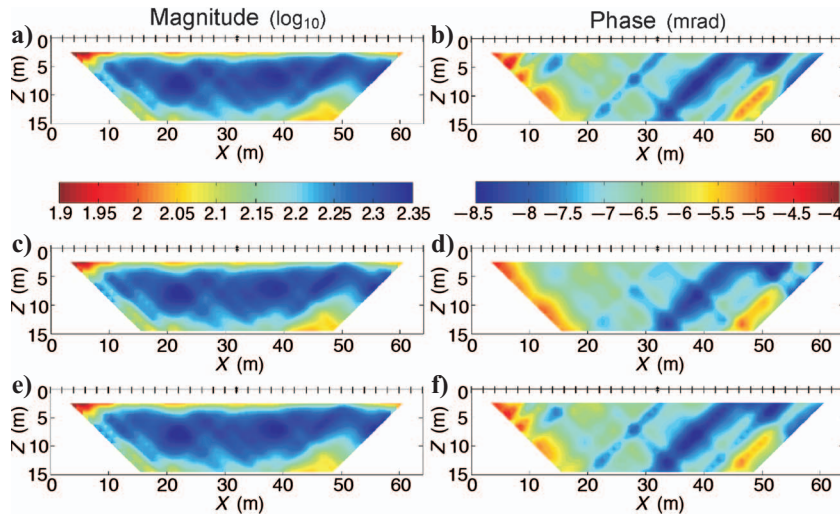


Figure 11. Pseudosections of magnitude (left, in  $\Omega\text{m}$ ) and phase (right, in mrad) of apparent complex resistivity data. (a and b) Measured data, (c and d) data predicted by the smoothness-constrained inversion result, and (e and f) data predicted by the inversion result obtained with SCF regularization.

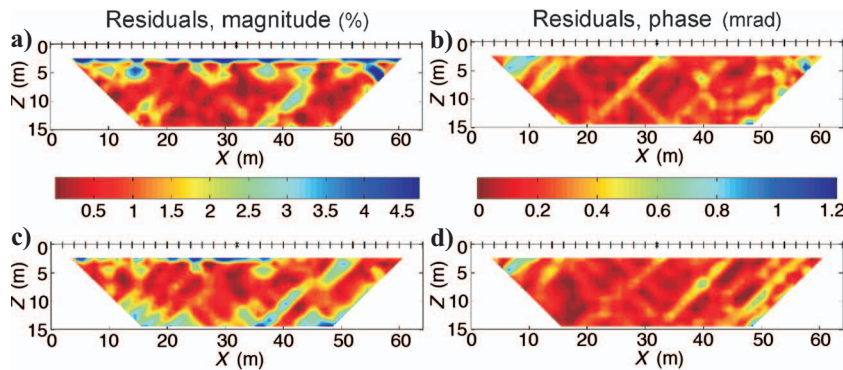


Figure 12. Distribution of residuals between measured apparent complex resistivity data and data predicted by the inversion result [(a and b) smoothness constraint, (c and d) SCF].

Figure 12 shows the difference between the measured data and the data predicted by the inversion result in standard pseudosection form. Even if the case is not as clear as in the first simple synthetic model (Figures 2 and 7), some differences in the data fit between the two regularization schemes are visible. For both regularization schemes, the spatial error distribution is not random, as would have been expected in the ideal case. However, the extreme deviations are larger and more clustered in the smoothness-constrained inversion result (Figure 12a and b), where high magnitude errors appear along the surface, and the phases are slightly more disturbed along the right boundary and at the upper left corner of the pseudosection. We therefore conclude that the SCF regularization result is also preferable from an error distribution point of view.

## CONCLUSIONS

We have proposed a new regularization scheme for the inversion of complex resistivity data by combining the ideas of the minimum gradient support and active constraint balancing. We have suggested that the control parameter be varied in order to obtain a continuous

transition between focused and smooth images. Our scheme may be considered a tool for exploring model space, i.e., finding different models that give an equally good data fit. Because the control parameter does not depend on survey geometry or discretization, it is also possible to use a fixed standard value that will result in a moderately focused image.

Our studies with synthetic data show that in the case of structures with sharp boundaries, SCF regularization is clearly superior to smoothness-constrained inversion. Not only does it provide a better reproduction of the true model, but the structure of the residual error is more randomly distributed. Additional studies have shown that the SCF inversion produces acceptable results when the true structure does not have sharp boundaries, although it has not been designed for such cases. Moreover, these studies indicate that the convergence and stability of the code is comparable to smoothness-constrained inversions. For the field example, the SCF inversion produced images that agreed well with the known average lithology.

The application of the SCF scheme has two implicit risks. The possibility of exploring model space might tempt the interpreter to select a desired result, and the sharp boundaries automatically produced by the inversion could be taken as an increased resolution, which would lead to an inaccurate determination of layer boundaries. It is therefore recommended, as for all interpretation procedures, that a priori information be incorporated whenever possible. Our scheme, although a useful alternative to smoothness-constrained inversion, does not reduce the interpreter's responsibility to apply the necessary care and avoid over-interpretation.

SCF regularization is particularly suited to structures with well-separated zones with moderate parameter variations. This is often the case in hydrogeologic applications, where lithologic boundaries between gravel, sand, and clay are well defined. In relatively homogeneous material with diffuse layer boundaries a smoothness-constrained inversion should be preferred, even though the SCF approach leads to acceptable results. We applied our scheme to IP data because our aim was to estimate hydraulic conductivities from the real and imaginary parts (or magnitude and phase, as shown in the figures) of complex electrical conductivity using existing empirical relationships. As illustrated in Figure 8, the benefits of SCF inversion could be particularly important for resolving small phase variations. Of course, SCF regularization may be suitable for inverting other types of geophysical data as well, particularly dc resistivity, electromagnetic, and magnetotelluric measurements.

For SIP data, the SCF regularization has already been successfully implemented for the simultaneous inversion of complex resistivity data recorded at different frequencies. This is performed with an a priori assumption on the frequency behavior of the intrinsic complex conductivities, such as the constant phase angle model or the Cole-Cole model.

## ACKNOWLEDGMENTS

This work was funded by the German Research Foundation DFG (project Ho1506/11-1,-2). The authors would like to thank Norbert Zisser for support during the field measurements and Tino Radic for useful advice on data acquisition. The comments of Frederic Nguyen on an earlier version greatly improved the manuscript. We would like to acknowledge the constructive comments of three anonymous reviewers.

## REFERENCES

- Auken, E., and A. E. Christiansen, 2004, Layered and laterally constrained 2D inversion of resistivity data: *Geophysics*, **69**, 752–761.
- Bertin, J., and J. Loeb, 1976, Experimental and theoretical aspects of induced polarization, vol. 1 and 2: Gebrüder Borntraeger.
- Blaschek, R., 2006, Aspekte der Inversion von Daten der Spektralen Induzierten Polarisation: Ph.D. thesis, University of Bonn.
- Blaschek, R., A. Hördt, and A. Kemna, 2006, Inversion of SIP data for Cole-Cole and constant-phase-angle relaxation model parameters: Proceedings of the Near Surface Section: 12th European Meeting of Environmental and Engineering Geophysics, EAGE.
- Börner, F. D., J. R. Schopper, and A. Weller, 1996, Evaluation of transport and storage properties in the soil and groundwater zone from induced polarization measurements: *Geophysical Prospecting*, **44**, 583–601.
- Chambers, J. E., M. H. Loke, R. D. Ogilvy, and P. I. Meldrum, 2004, Noninvasive monitoring of DNAPL migration through saturated porous medium using electrical impedance tomography: *Journal of Contaminant Hydrology*, **68**, 1–22.
- DeGroot-Hedlin, C., and S. Constable, 1990, Occam's inversion to generate smooth, two-dimensional models from magnetotelluric data: *Geophysics*, **55**, 1613–1624.
- , 2004, Inversion of magnetotelluric data for 2D structure with sharp resistivity contrasts: *Geophysics*, **69**, 78–86.
- Hördt, A., R. Blaschek, A. Kemna, J. Suckut, and N. Zisser, 2004, Hydraulic conductivity estimation from spectral induced polarization data — a case history: 10th European meeting of environmental and engineering geophysics, EAGE.
- , 2005, Hydraulic conductivity from spectral induced polarisation data — a case history: 18th Annual meeting, SAGEEP, Expanded Abstracts, 226–235.
- Hördt, A., R. Blaschek, A. Kemna, and N. Zisser, 2007, Hydraulic conductivity estimation from induced polarisation data at the field scale — the Krauthausen case history: *Journal of Applied Geophysics*, **62**, 33–46.
- Kemna, A., 2000, Tomographic inversion of complex resistivity — theory and application: Ph.D. thesis, Bochum Ruhr-University.
- Kemna, A., and A. Binley, 1996, Complex electrical resistivity tomography for contaminant plume delineation: Proceedings of the European Section, 2nd Meeting on Environmental and Engineering Geophysics, Environmental and Engineering Geophysical Society, 196–199.
- Kemna, A., A. Binley, A. Ramirez, and W. Daily, 2000, Complex resistivity tomography for environmental applications: *Chemical Engineering Journal*, **77**, 11–18.
- Kemna, A., A. Binley, and L. Slater, 2004, Crosshole IP imaging for engineering and environmental applications: *Geophysics*, **69**, 97–107.
- Kemna, A., E. Räckers, and L. Dresen, 1999, Field applications of complex resistivity tomography: 69th Annual International Meeting, SEG, Expanded Abstracts, 331–334.
- LaBrecque, D. J., M. Miletto, W. D. Daily, A. L. Ramirez, and E. Owen, 1996, The effects of noise on Occam's inversion of resistivity tomography data: *Geophysics*, **61**, 538–548.
- Last, B. J., and K. Kubik, 1983, Compact gravity inversion: *Geophysics*, **48**, 713–721.
- Loke, M. H., I. Acworth, and T. Dahlin, 2003, A comparison of smooth and blocky inversion methods in 2D electrical imaging surveys: *Exploration Geophysics*, **34**, 182–187.
- Newman, G. A., and D. L. Alumbaugh, 1997, Three-dimensional massively parallel electromagnetic inversion — I. Theory: *Geophysical Journal International*, **128**, 345–354.
- Oldenburg, D. W., P. R. McGillivray, and R. G. Ellis, 1993, Generalized subspace methods for large-scale inverse problems: *Geophysical Journal International*, **114**, 12–20.
- Portniaguine, O., 1999, Image focusing and data compression in the solution of geophysical inverse problems: Ph.D. thesis, University of Utah.
- Portniaguine, O., and J. P. Castagna, 2004, Inverse spectral decomposition: 74th Annual International Meeting, SEG, Expanded Abstracts, 1786–1789.
- Portniaguine, O., and M. S. Zhdanov, 1999, Focusing geophysical inversion images: *Geophysics*, **64**, 874–887.
- , 2002, 3-D magnetic inversion with data compression and image focusing: *Geophysics*, **67**, 1532–1541.
- Radic, T., 2004, Elimination of Cable effects while Multichannel SIP measurements: 10th European Meeting of Environmental and Engineering Geophysics, EAGE, Extended Abstracts.
- Radic, T., D. Kretschmar, and E. Niederleithinger, 1998, Improved characterisation of unconsolidated sediments under field conditions based on complex resistivity measurements: 4th European Meeting of Environmental and Engineering Geophysics, EAGE, Extended Abstracts.
- Slater, L. D., and D. R. Glaser, 2003, Controls on induced polarization in sandy unconsolidated sediments and application to aquifer characterization: *Geophysics*, **68**, 1547–1558.
- Slater, L., and D. P. Lesmes, 2002, Electrical-hydraulic relationships observed for unconsolidated sediments: *Water Resources Research*, **38**; <http://dx.doi.org/10.1029/2001WR001075>.
- Smith, T., M. Hoversten, E. Gasperikowa, and F. Morrison, 1999, Sharp boundary inversion of 2D magnetotelluric data: *Geophysical Prospecting*, **47**, 469–486.
- Sumner, J. S., 1976, Principles of induced polarization for geophysical exploration: Elsevier Science.
- Telford, W. M., L. P. Geldart, and R. E. Sheriff, 1990, Applied Geophysics: Cambridge University Press.
- Tikhonov, A. N., and V. Y. Arsenin, 1977, Solution of ill-posed problems: V. H. Winston and Sons.
- Vereecken, H., U. Döring, H. Hardelauf, U. Jaekel, U. Hashagen, O. Neuen-dorf, H. Schwarze, and R. Seidemann, 2000, Analysis of solute transport in a heterogeneous aquifer, The Krauthausen field experiment: *Journal of Contaminant Hydrology*, **45**, 329–358.
- Yi, M.-J., J.-H. Kim, and S.-H. Chung, 2003, Enhancing the resolving power of least-squares inversion with active constraint balancing: *Geophysics*, **68**, 931–941.
- Yoshioka, K., and M. S. Zhdanov, 2005, Three-dimensional nonlinear regularized inversion of the induced polarization data based on the Cole-Cole model: *Physics of the Earth and Planetary Interiors*, **150**, 29–43.
- Zhdanov, M. S., 2002, Geophysical inverse theory and regularization problems: Elsevier Science.
- Zhdanov, M. S., and E. Tolstaya, 2004, Minimum support nonlinear parameterization in the solution of a 3D magnetotelluric inverse problem: *Inverse Problems*, **20**, 937–952.